Supplementary material for "*Electromagnetic constraints for subduction zones beneath the northwest Borborema province: Evidence for Neoproterozoic island arc-continent collision in northeast Brazil*"

Data acquisition and processing

For this study, the horizontal components of the electric field (Ex and Ey) and the horizontal and vertical components of the magnetic field (Hx, Hy and Hz) were recorded at 52 sites along two SE-NW parallel profiles (with a 80-90 km offset between them) (Fig. 1 in the main text). Profile A consists of 34 broadband sites (17 of which also included long-period data at each second site) in a total length of about 500 km and profile B has a length of 360 km with 18 broadband sites (9 with long-period) on it. Within each profile the sites are at approx. 15-20 km intervals and the data were gathered from different field campaigns carried out during the years 2007-2010. Commercial single-station (not remote-referenced) MT systems (Metronix ADU-06) were used to record broadband data (periods from 0.001 to 1024 s) and commercial remote-referenced MT systems (Phoenix LRMT and Lviv Lemi 417) were used for long-period data (period range from 10 to about 13,000 s). Recording time at each station was at least 2 days with the broadband systems and at least 2 weeks with the long-period systems. Long period data were acquired immediately after the broadband data, using the

same electrode array layout. As a consequence, it was not necessary to correct for static shift between both measurements.

As noise levels during the surveys were generally low, reliable broadband response function estimates were obtained at most sites in the period range 0.001 to 410 s (see Figs. DR5-DR7). Some scatter at specific short periods are associated with ambient cultural noise and, in the period range of 1-10 s, attributable to the MT dead-band of low-amplitude signals. These corrupted responses were removed prior to analysis and interpretation. Due to larger values of the noise/signal ratios, sites over the Archean Tróia-Tauá massif showed a significant decrease in data quality, with station 3 in profile B only producing usable data up to 4 s and another station between the stations 2 and 3 in the same profile being completely discarded. In addition, there were recording failures in the electric field of station 12 in profile B. Due to the low signal amplitude of the longer periods throughout the recording period (extremely low solar activity during solar minimum, aggravated by the low amplitude of geomagnetic variations at these very low geomagnetic latitudes; e.g., Trivedi et al., 1997), signal-to-noise ratio was unusually low and only at a few sites were the responses extended outside the range given by the broadband equipment.

Dimensionality and geoelectric strike

Groom-Bailey (GB) tensor decomposition (Groom and Bailey, 1989) gives acceptable fits to the measured data at most sites, with small chi-squared misfits

and shear and twist angles less than 20^{o}. This is taken as indicative that the geoelectric structure can be represented by the 3D/2D approximation of the GB decomposition. An additional analysis using the WALDIM code (Marti et al., 2005) showed similar results to those of the GB decomposition.

Figure DR1 displays the strike directions in two period bands obtained independently at each station. The strikes are weighted by the phase difference between the off-diagonal elements of the impedance tensor. In short periods, penetrating upper crustal depths, strikes are generally oriented NE-SW, consistent with surface tectonic features. A significant number of stations shows very small phase difference (less than 10^{o}), an indication that their responses are less dependent on rotation. At longer periods, sampling lower crust and upper mantle, phase difference generally increases, pointing to multidimensional structure at deeper depths. However, the strike directions are nearly the same of those in short periods so that a single strike direction can be adopted for both the crust and mantle. The multisite, multifrequency tensor-decomposition code of McNeice and Jones (2001) was used to determine the strike that best fits all the sites at each profile. The calculated geoelectric strike angles were $N42^{o}E$ (or $N48^{o}W$ due to the inherent 90^{o} ambiguity in strike determination) for profile A and $N40^{o}E$ (or $N50^{o}W$) for profile B. The NE strike is almost certainly correct because it agrees with the main direction of the Brasiliano/Pan-African deformation in the area.

An independent constraint on dimensionality and geoelectric strike is given by the magnetic transfer functions (Weidelt and Chave, 2012). They can be

plotted as induction arrows which are orthogonal to the strike in a two-dimensional (2D) setting and their real parts point toward zones of enhanced conductivity when reversed (Parkinson convention). The real induction arrows for four periods are shown in Figure DR2. At the shortest period (0.4 s) the arrows have a complex pattern, affected by local structures at shallow depths close to the sites. At 4.5 s, the magnitudes of the arrows decrease at most of the stations but they show an outward reversal of direction across the Jaguaribe subdomain in profile A, suggesting the existence of a significant geoelectrical anomaly beneath this unit. At 37 s, the arrows at the western end of profile A start to show the influence of coastal effects, pointing roughly perpendicular to the coastline. Close to the center of the same profile, arrows point perpendicular to the MT transect, indicating an off-profile anomaly in the NE, whereas at its eastern end the geoelectrical anomaly beneath the Jaguaribe is emphasized. On the other hand, profile B is much less affected by off-profile conductors with most of the arrows oriented parallel to the profile, in the NW direction, and giving support to a predominantly NE strike direction. At the western end of this profile, the arrows appear affected by structures outside the profile under the Parnaíba basin. Results at 410 s are similar to those in 37 s, with enhanced coast effects at the western sites of profile A. Along profile B, the coast effect is only sensed by the sites to the west of the Transbrasiliano lineament, but along the rest of the profile most of the arrows continue to be oriented NW. In summary, the induction arrows analysis shows that the study area is less 2D in some localized areas and more sensitive to off-profile structures than inferred from the GB decomposition. With

the exception of long periods for a few sites over the Parnaíba basin, profile B allows a 2D approach with an N40^{o}E strike direction.

Evaluating Coast Effects on MT Transfer Functions

The coast effect is related to the sharp contrast in conductivity between the relatively more resistive land and the more conductive ocean at shallow depths which will produce an electric current concentration in the conducting sea water flowing parallel to the coastline (Parkinson, 1964; Schmucker, 1970; Fischer, 1979; Parkinson and Jones, 1979). The magnitude of the coast effect will depend on different factors (subsurface geology, contrast in conductivity between the sea water and subsurface layers, depth of the ocean, frequency of the signal and distance of the MT site from the coast). For soundings onshore, it will lead to a splitting in the apparent resistivity curves at long periods, with higher values in the mode with the electric field parallel to the coast (TM mode in our case) and lower values in the mode with the electric field perpendicular to the coast (TE mode in our case). As a consequence, MT data analysis from coastal areas must account for the effects generated by the presence of induced currents flowing in the sea water at the coastline.

A 3D model study was performed in order to check the coastal effects on the Borborema data set and to define the period interval not influenced by the sea at each site. A 3D mesh was created with the sea water represented by resistivity values of 0.3 Ωm, extending to depths given by the available local

bathymetry, and a 1D layered model, derived from MT soundings far away from the coastline, representing the Earth resistivity both landward and seaward beneath the ocean. Model accuracy was tested with available induction arrows and showed that the conductance of the sediments on the shelf is only important along the north-eastern continental corner (location of the onshore-offshore Potiguar basin). A compilation of the results is presented in Figure DR3, using as example a site in profile A at about 70 km landward from the coast (shown as a white dot in Fig. DR3c). The 1D model is presented in Figure DR3a and a comparison of the curves with and without an ocean is shown in Figure DR3b. There is no difference in the response at short periods, but beyond a certain period (in this example at about 60 s for the TE apparent resistivity, 200 s for the TM apparent resistivity, 20 s for the TE phase, and 90 s for the TM phase) the curves differ significantly as a consequence of the coast effect.

We estimated the coast effect through the percentage deviation between the responses with and without an ocean, calculated in each cell of the 3D model for all periods measured. Figure DR3c shows a map with the calculated deviation for the apparent resistivity in the period of 410 s (upper limit of the broadband data), considering the electric field in the EW direction (parallel to the coastline of NW Borborema). Taking into account the location of our MT soundings, this is the polarization at which the largest coast effect is expected (for the eastern edge of the province the largest effect would be generated by the electric field in the NS direction). Similar calculations were performed for both polarizations in the entire recorded period range. For the 2D inversion, data were discarded that showed

deviations above the error floor used (10% in apparent resistivity and 5% in phase).

Modeling

Due to different boundary conditions at interfaces, the three components of the data (TE and TM mode transfer functions and tipper) are sensitive to different aspects of the subsurface structures. Therefore, a joint inversion of the components is normally needed to obtain a reliable resistivity model of the subsurface. The choice of the components used for joint inversion was based on model roughness and fitting of the measured data with an acceptable root main square (RMS) misfit, mainly considering the effects produced by off-profile 3D structures. After numerous tests to achieve a best-fitting and reliable final model, it was observed that the addition of the tipper data in the 2D inversion of profile A caused the RMS misfit to increase significantly. This was mainly associated with stations located in the central part of the profile, where induction arrows do not point along the profile as expected in a 2D case. The models themselves showed little structural change between the TE-TM models and the TE-TM-Tzy models (where Tzy means the vertical magnetic field component Bz being related to the induced electric currents flowing parallel to the strike direction), an indicator that the tipper was not changing the model. Consequently, tipper data were not included in the inversion of this profile. On the other hand, inclusion of the TE mode in the inversion of profile B caused an increase of the total RMS values

and led to very complicated and rough models, with unrealistic discrete conductors located throughout the models. It was found that the TE-TM and the TM-Tzy gave the most reliable images of the subsurface for profiles A and B, respectively, considering both the roughness of the model and the data misfit.

Field data consisted of transfer functions responses for the 52 stations at mostly 38 periods extending from 0.0011 to 410 s. Unreliable data with large scatter or internally inconsistent through a Rho+ analysis (Parker and Booker, 1996) were removed from the dataset prior to inversion. The data were initially inverted for the TM mode alone because this mode is less affected by off-profile structures and less liable to static shift effect. A larger error floor was used for the resistivities, thus emphasizing phase fitting. The resulting model was used as the starting model for the joint inversion of the TM and TE/tipper data. Successively the error floors were reduced and static shift coefficients determined so that the final inversion was run with error floors of 5% in the phases, 10% in the apparent resistivities, and 0.02 in the tipper. The starting models were either uniform half-spaces or a layered half-space determined from 1D inversion of the geometric mean of each site, and all gave essentially the same final resistivity models. The preferred 2D inversion models shown in Figure 2 of the main text were obtained considering a trade-off between the roughness of the model and the data misfit. The REBOCC program seeks the minimum possible structure (given by a model norm) for a given level of misfit (see Siripunvaraporn and Egbert, 2000). Figure DR4 illustrates the trade-off between the RMS misfit of the model to the data and the model norm for the final inversion of profile A. The final models were derived

using a starting half-space resistivity of 100 Ωm and allowed acceptable misfits between observations and model predictions with overall RMS of 1.79 for profile A and 1.63 for profile B, related to the assumed error floors. Comparisons between the data and model responses for the whole dataset can be found in Figures DR5-DR7.

Model appraisal

Because of the non-uniqueness of solutions to the inverse problem, there are an infinite number of models that can fit the MT data. The robustness of the models was tested with different initial models, varying the inversion parameters used in the inversion code, and using different error floors around the proposed values. As an example, Figure DR8 shows 2D inversion models for both profiles when all data components (TE, TM and Tzy) are considered. The same relevant features of the preferred models in Figure 2 were obtained.

In addition, a nonlinear sensitivity study of the models was carried out to test the sensitivity of the data to the most striking features of the models. This was made by constructing representative resistivity models by adding or removing structures from the original models, computing the altered model responses through forward modeling, and comparing the misfits between the final inversion model responses and the altered model responses with the measured data.

Figures DR9-DR11 exemplify the results of nonlinear sensitivity tests on some prominent features of the final models. Figure DR9 is the same as Figure 2, but indicating the anomalous features to be discussed in Figure DR11. Figure DR10 shows the edited model of profile B for testing the conductive structures C2 and C3. The regions where the conductors are located (red rectangles) are set to a uniform 500 Ωm (background resistivity around the conductive anomalies).

To test data sensitivity to model feature C1, the resistivity of the vertical conductor was changed to a more resistive value (300 Ωm) that closely approximates the background resistivity of middle and lower crust in the model. The plot in Figure DR11a illustrates that at periods longer than 10 s the calculated forward responses of the altered model are clearly different from the modeled or observed data at the most affected site, especially for the TE mode. This result indicates that the conductive feature C1 is a robust model feature that is required by the data. In Figure DR11b is tested the possibility that the resistive feature R1 could extend laterally and upwardly like the resistive structure at upper mantle depths in profile B. Effects would only be felt at periods longer than 100 s, but RMS misfit is nearly the same for the altered and the original model. Unfortunately, data fitting is not accurate enough in the TE phase (the most affected by the change) to allow discrimination between the original and the edited models. In this case, the forward modeling prevents any conclusion regarding the possible extension of resistor R1. Figures DR11c and DR11d show tests for the conductive features C2 and C3 of profile B. As already discussed, the resistivity of the conductors was changed to the values of the background

resistivity of lower crust and upper mantle in the model. The TM mode shows little sensitivity to the change, indicating that this mode is insensitive to both conductivity structures. On contrary, the tipper responses show significant misfits at periods longer than 20 s. For the conductor C2 the altered model does not fit the observed real part of the tipper data at the longest periods, suggesting that the feature is required by the data. However, for the conductor C3 the test is inconclusive because both the original and the altered models provide poor data fitting at the critical periods.

The most meaningful features of the MT models are the presence of two resistive structures R2 and R3 in the geoelectric model for profile B. The structures dip in opposite directions into the lower crust and merge into each other in the upper mantle. The crustal part of these structures has resistivities in the range 1000-3000 Ωm, whereas their mantle part has resistivity larger than 10,000 Ωm. Testing data sensitivity to these dipping resistors is required because MT data resolve conductive layers better than resistive layers. In the tests, the resistivity of both resistors in the crust was reduced to the crustal background resistivity in the area (300 Ωm) and forward responses of the altered model were calculated. Figures DR11e and DR11f show that the high resistivity values of the dipping structures are constrained mainly by the TM data. Another approach to test data sensitivity to the dipping resistors was through constrained inversion. Initially, the edited model (with the resistivity of the resistors reduced to the crustal background resistivity) was used as a starting model in the inversion process. The inversion recovered the original resistivity values and fitted the data

with similar RMS. After that the edited model was used again as a starting model, but this time keeping the edited region fixed during the inversion. In this case, the inversion tried to accommodate the change by increasing the resistivities around the edited region, but the RMS increased significantly at the representative sites (located around the edited region). It was concluded that the resistive dipping features are required by the MT data.

Other model tests were conducted to evaluate the maximum depth of sensitivity of the models to the data. Following the procedure described in Padilha et al. (2013), a perfect conductor (resistivity of 10^{-8} Ωm) half-space was initially placed at 200 km depth and the forward response of the edited models was calculated with the RMS data misfit compared to the misfit of the original inversion models at each site. The depth to the conductor was progressively shallowed by 20 km increments until a depth at which the RMS misfit increased, thus defining the maximum depth of sensitivity of the models. The same exercise was performed with a perfect resistor (10^{8} Ωm) half-space giving essentially the same results as the perfect conductor. The estimated maximum depths of sensitivity of the models for 2D interpretation beneath each site are presented in the models of Figure 2. With the exception of regions where data at long periods were discarded due to poor data quality (Tróia-Tauá massif) or to prevent coastal effects (western end of profile A) and in the region of the major conductor seen on profile A, the models can be interpreted to the maximum depth shown in Figure 2 (100 km).

Additional References

Fischer, G., 1979. Electromagnetic induction effects at an ocean coast, Proceedings of the IEEE 67, 1050–1060.

Groom, R.W., Bailey, R.C., 1989. Decomposition of magnetotelluric impedance tensor in the presence of local three-dimensional galvanic distortion. Journal of Geophysical Research, 94, 1913–1925.

Marti, A., Queralt, P., Jones, A.G., Ledo, J., 2005. Improving Bahr's invariant parameters using the WAL approach. Geophysical Journal International, 163, 38–41.

Padilha, A.L., Vitorello, I., Pádua, M.B., 2013. Deep conductivity structure beneath the northern Brasília belt, central Brazil: Evidence for a Neoproterozoic arc-continent collision. Gondwana Research, 23, 748–758.

Parker, R.L., Booker, J.R., 1996. Optimal one-dimensional inversion and bounding of magnetotelluric apparent resistivity and phase measurements. Physics of the Earth and Planetary Interiors, 98, 269–282.

Parkinson, W. D., 1964. Conductivity anomalies in Australia and the ocean effect. Journal of Geomagnetism and Geoelectricity, 15, 222-226.

Parkinson, W.D., Jones, F.W., 1979. The geomagnetic coast effect. Reviews of Geophysics, 17, 1999–2015.

Schmucker, U., 1970. Anomalies of geomagnetic variations in the south-western United States. Bulletin of the Scripps Institute of Oceanography 13, 165 pp.

Trivedi, N.B., Arora, B.R., Padilha, A.L., Da Costa, J.M., Dutra, S.L.G., Chamalaun, F.H., Rigoti, A., 1997. Global Pc5 geomagnetic pulsations of March 24, 1991 as observed along the American sector. Geophysical Research Letters 24, 1683-1686.

Weidelt, P., Chave, A.D., 2012. The magnetotelluric response function. In: Chave, A.D., Jones, A.G. (eds.), *The Magnetotelluric Method: Theory and Practice*. Cambridge University Press, Cambridge, Chapter 4, pp. 122-164.

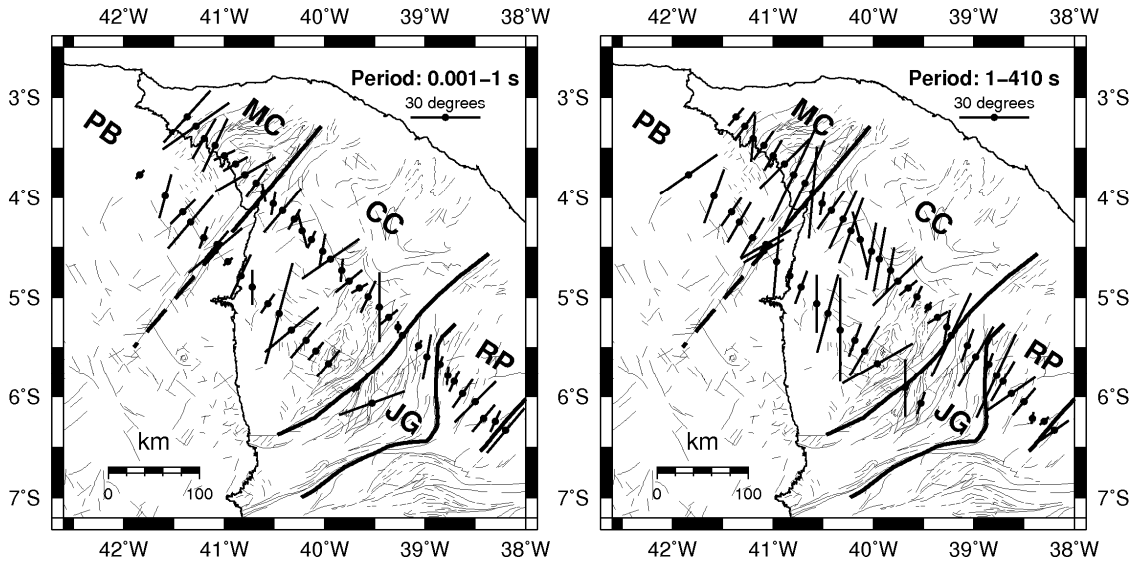

Figure DR1: Strike directions at each station in period bands 0.001-1 s and 1-410 s (GB decomposition). The lengths of the bars are proportional to the average phase difference over the band between the conductive (strike) and resistive directions. See Figure 1 in the main text for description of the geological units.

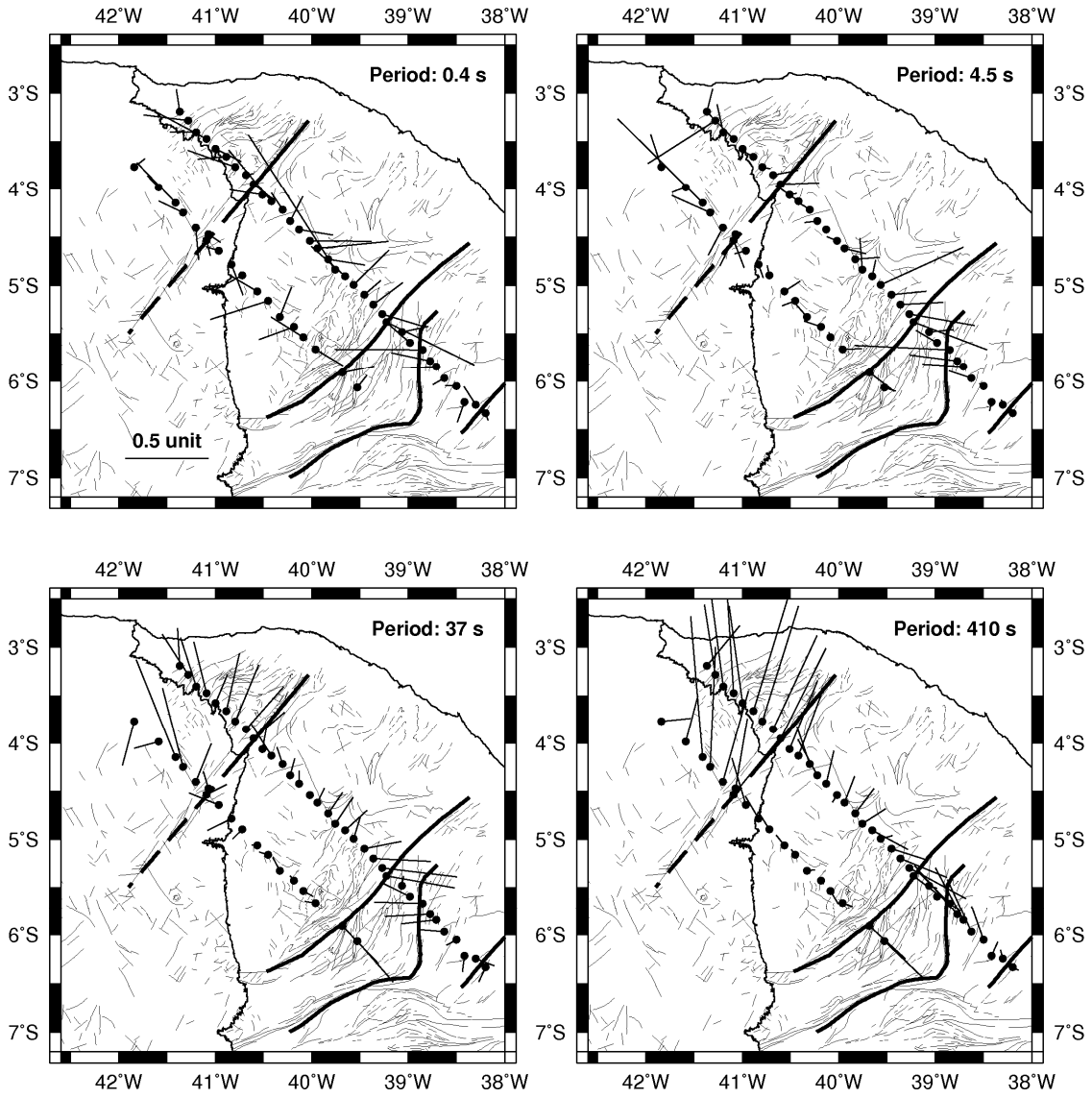

Figure DR2: Reversed real induction arrows for periods 0.4, 4.5, 37 and 410 s.

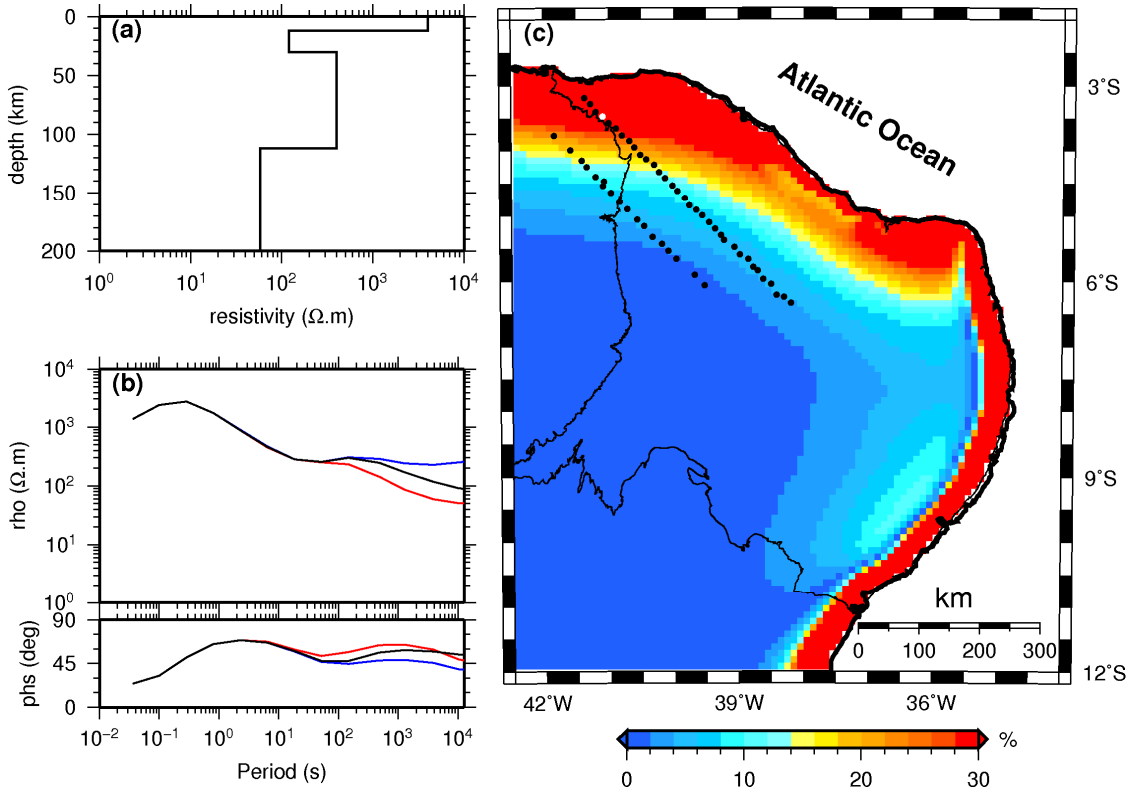

Figure DR3: Evaluating coastal effects on the Borborema data set through 3D modeling (see text for discussion). (a) 1D model used to represent Earth resistivity, derived from MT soundings far away from the coastline; (b) MT curves calculated without the ocean (black lines) and with the ocean (blue lines correspond to the electric field in the NS direction, red lines to the electric field in the EW direction); (c) Percentual deviation between the responses with and without the ocean for the apparent resistivity in the period of 410 s and electric field in the EW direction.

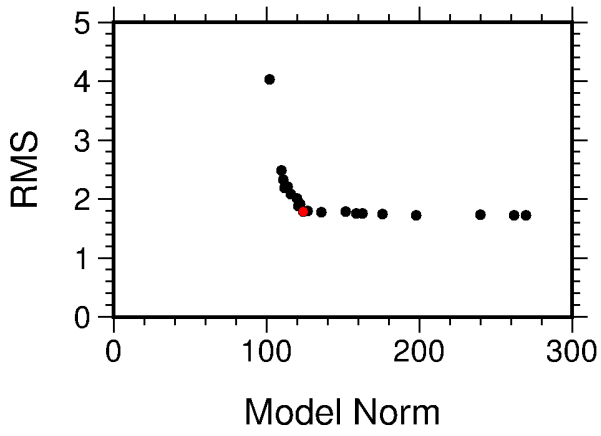

Figure DR4: L-curve between the RMS misfit and the model norm for the final inversion run of profile A. The chosen result is given by the red dot.

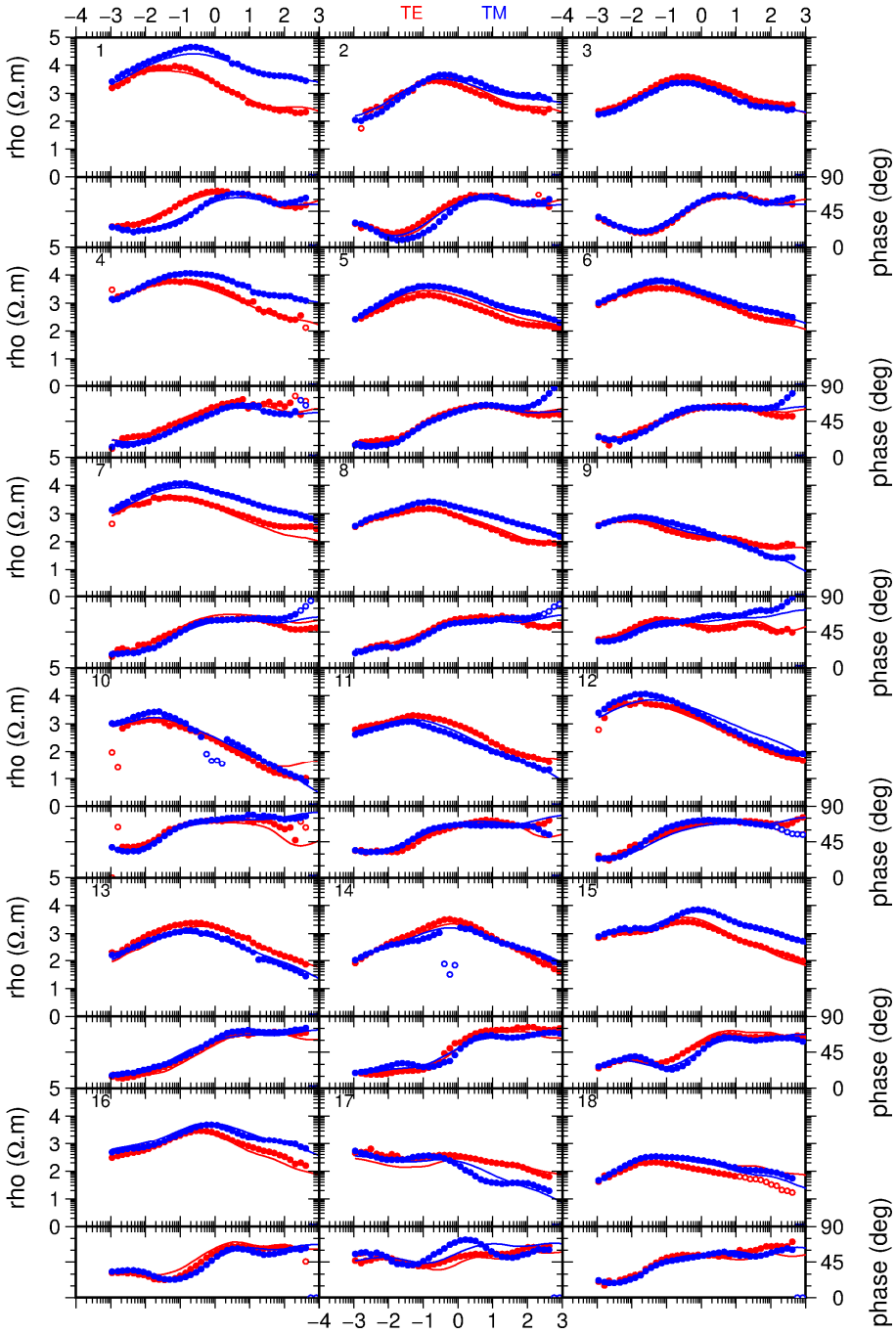

continue next page

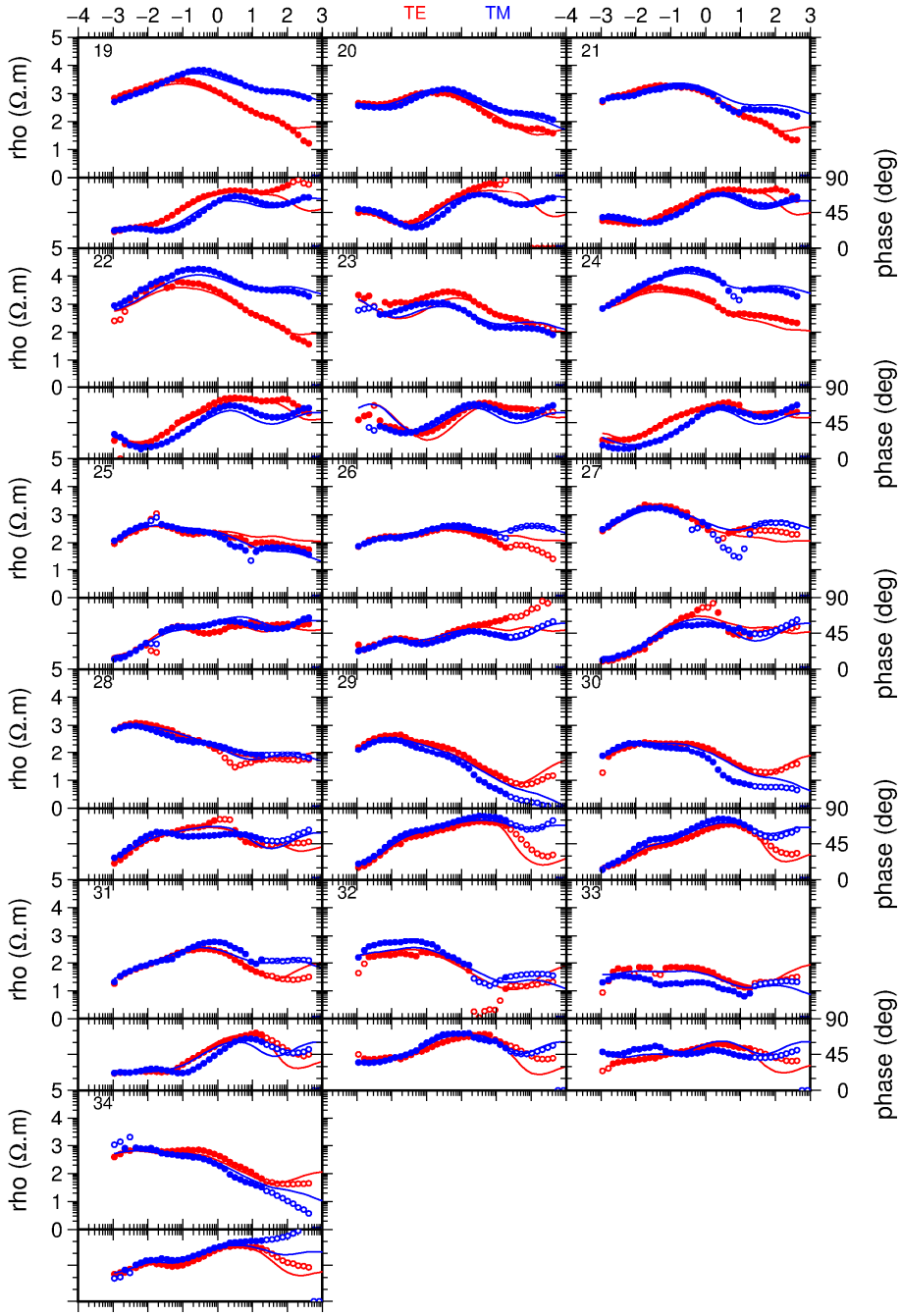

Figure DR5: A comparison of measured TE (red) and TM (blue) apparent resistivity and phase with model responses (continuous lines) for all stations along profile A. Data with open symbols were not used in the inversion. Site locations are presented in Figure 1 of the main text.

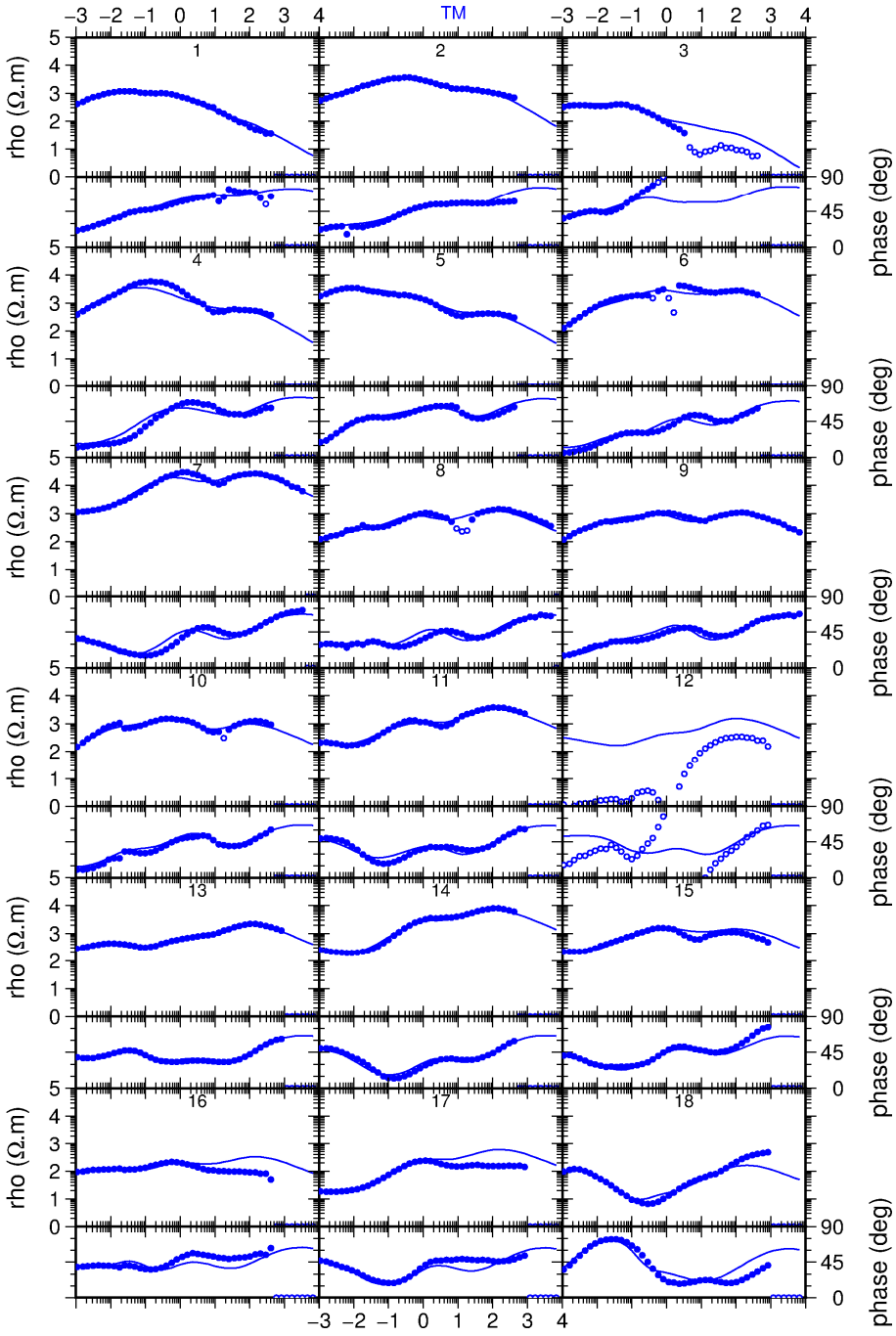

Figure DR6: The same as Figure DR5 for the TM mode along profile B.

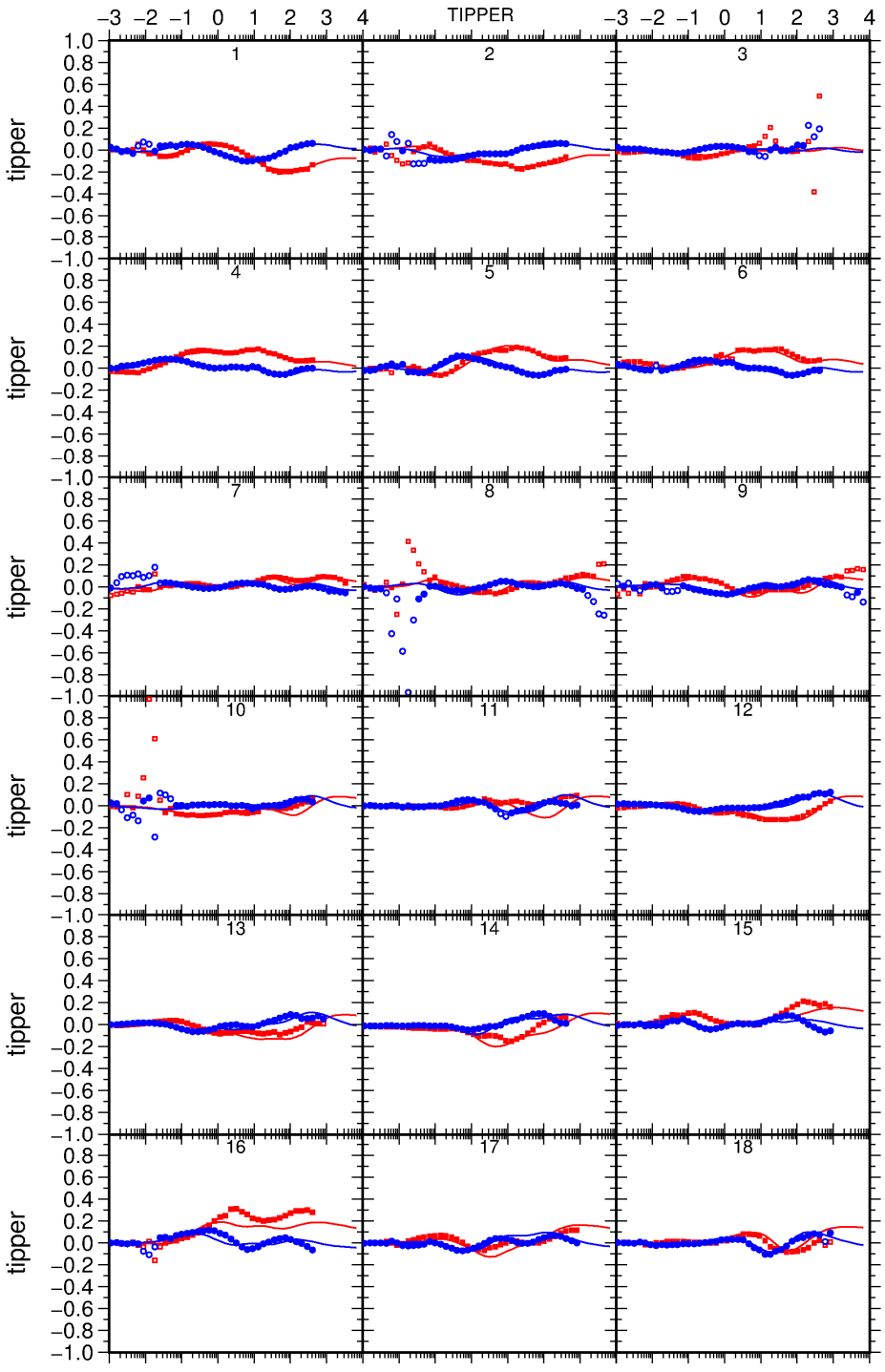

Figure DR7: The same as Figure DR5 for the real (red) and imaginary (blue) tipper components along profile B.

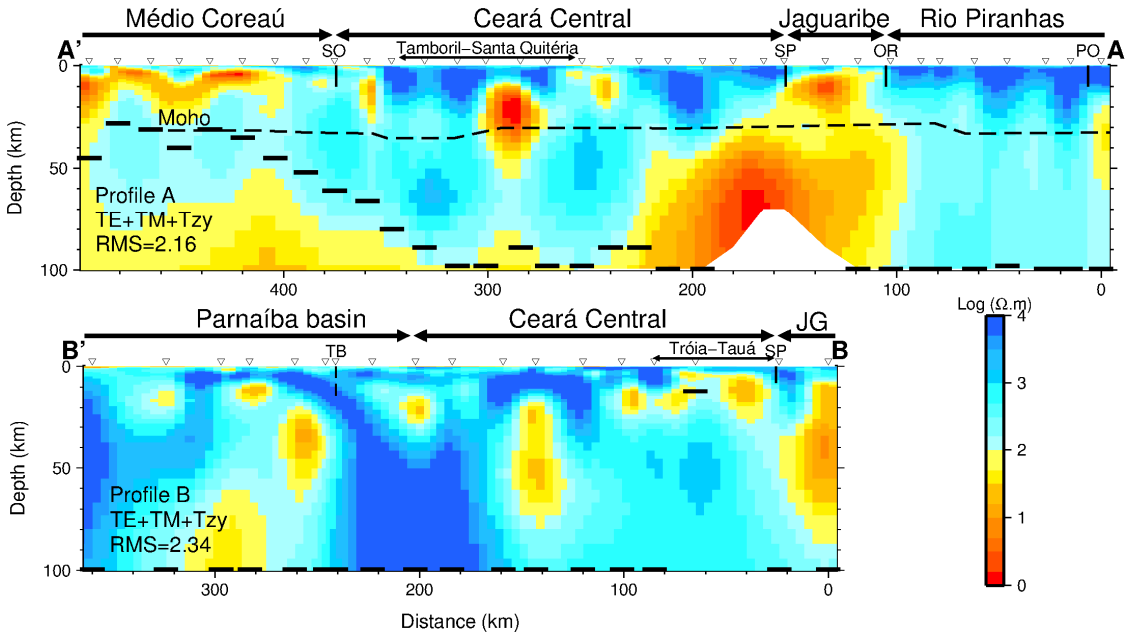

Figure DR8: 2D resistivity models for profiles A and B obtained by joint inversion of all data components (TE, TM and Tzy). Main features are the same as in Figure 2, but the RMS increase.

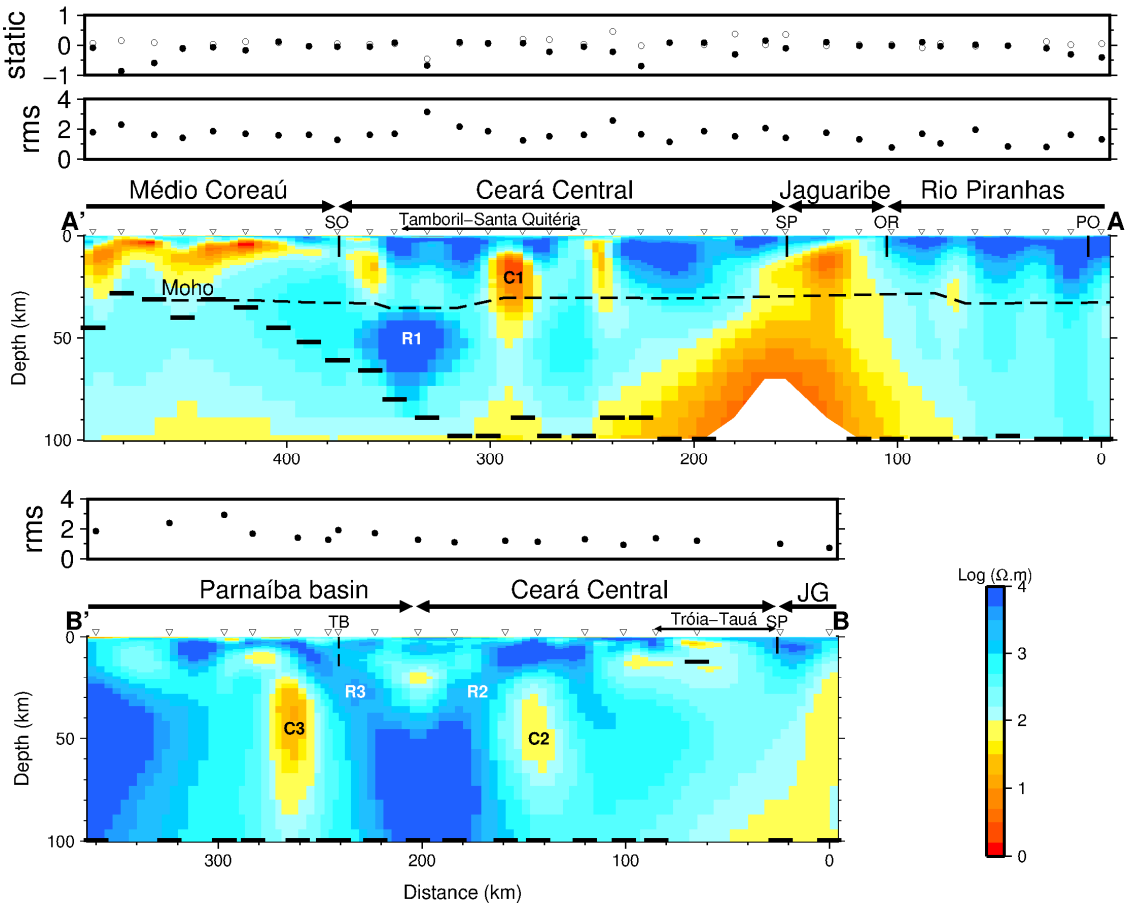

Figure DR9: 2D models of Figure 2 with the anomalous features to be discussed in Figure DR11 (conductors C1-C3; resistors R1-R3). RMS errors of single stations for both profiles and calculated static shifts coefficients for profile A (closed symbols for TE mode, open symbols for TM mode) are also shown.

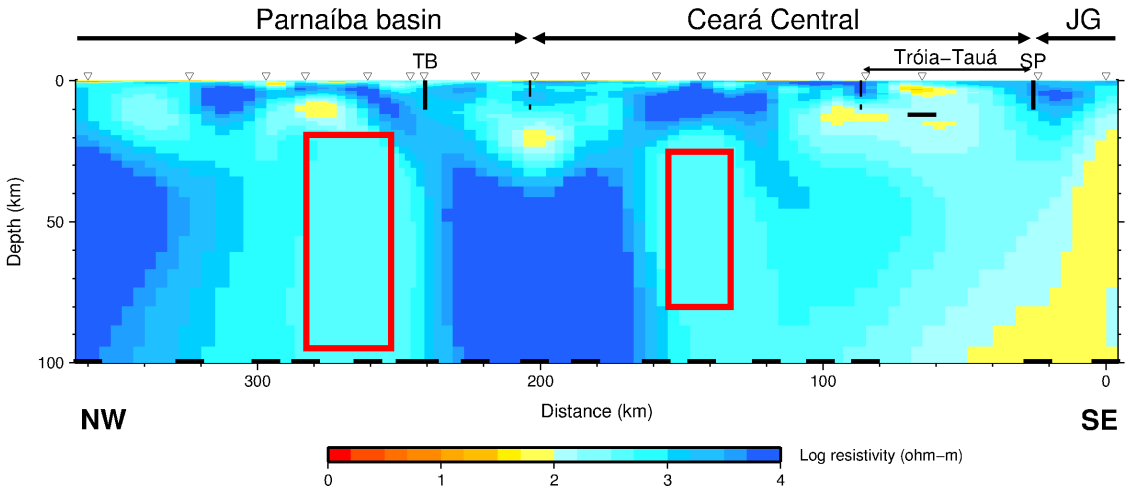

Figure DR10: Edited model of profile B for a resolution study of anomalies C2 and C3.

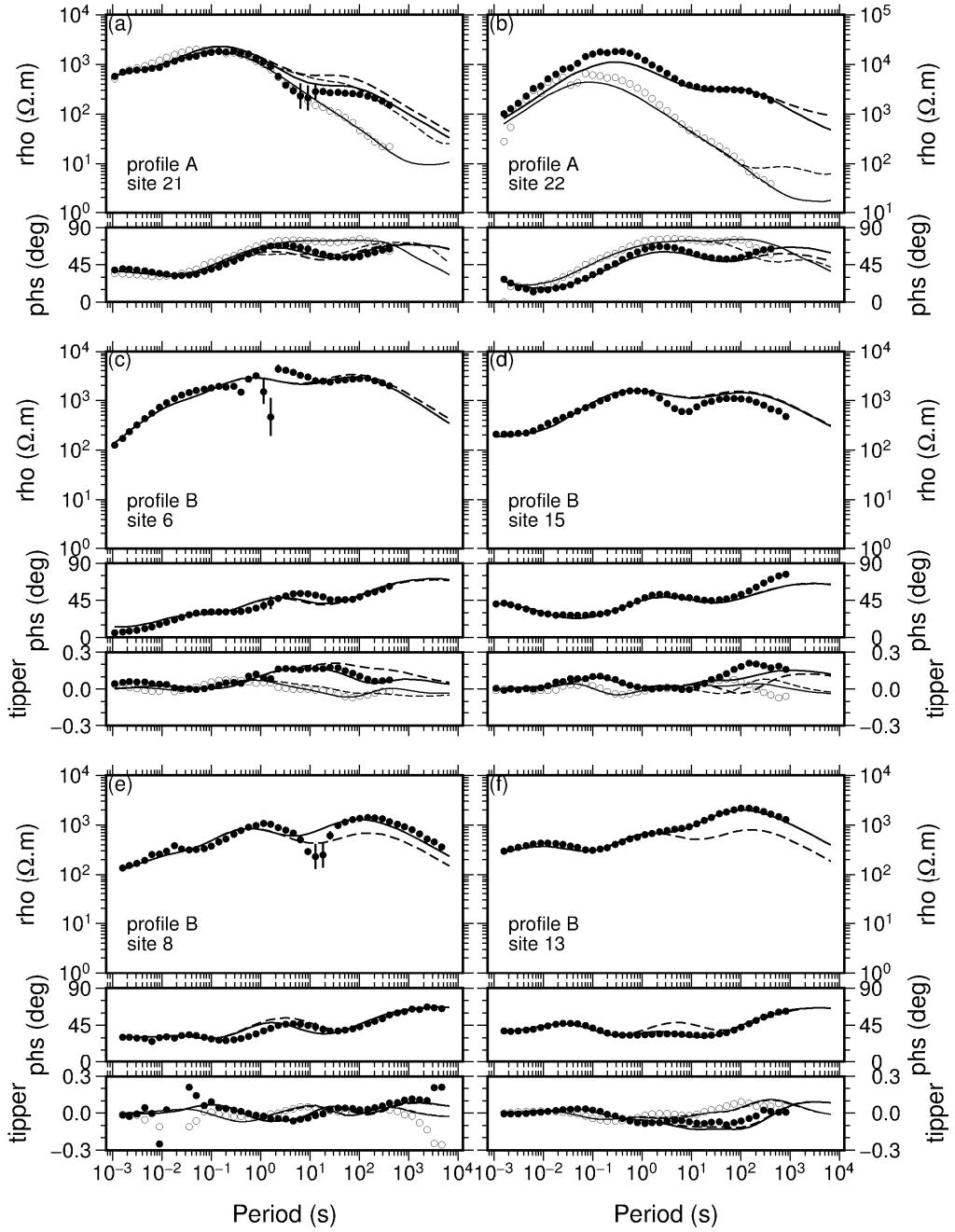

Figure DR11: Nonlinear sensitivity tests on features shown in Figure DR8. TE and Imaginary Tipper are shown with open symbols, TM and Real Tipper with closed symbols. (a) C1; (b) R1; (c) C2; (d) C3; (e) R2; (f) R3. See text for discussion.